

SPECIAL ISSUE ARTICLE

A thermodynamically consistent phase-field model for viscous sintering

Qingcheng Yang¹  | Arkadz Kirshtein² | Yanzhou Ji¹ | Chun Liu³ | Jie Shen⁴ | Long-Qing Chen^{1,2}

¹Department of Materials Science and Engineering, Penn State University, State College, Pennsylvania

²Department of Mathematics, Penn State University, University Park, Pennsylvania

³Department of Applied Mathematics, Illinois Institute of Technology, Chicago, Illinois

⁴Department of Mathematics, Purdue University, West Lafayette, Indiana

Correspondence

Qingcheng Yang, Department of Materials Science and Engineering, Penn State University, State College, PA.
Email: qzy25@psu.edu

Funding information

Department of Energy through ARPA-E, Grant/Award Number: DE-AR0000766; National Science Foundation, Grant/Award Number: DMS-1720442, DMS-1759536; Air Force Office of Scientific Research, Grant/Award Number: FA9550-16-1-0102; The Hamer Foundation for the Hamer Professorship

Abstract

A thermodynamically consistent phase-field model for viscous sintering is proposed. It is based on an energetic variational formulation that allows the governing equations to be analytically derived from a defined energy law. The conservation of mass is satisfied through the incompressibility assumption and the assumption that mass density is uniform initially within the particle compact while the balance of linear momentum is formulated from an energy dissipation law. The morphological changes of particles are described by the temporal and spatial evolution of a phase-field variable governed by a modified Cahn-Hilliard equation, and the motion of viscous mass flow is controlled by the Stokes equation incorporating the surface tension effect. The application of the phase-field model is illustrated by examining the effect of particle shape, initial contact angle and rearrangement effects on viscous sintering.

1 | INTRODUCTION

Sintering is a process in which thermal energy is utilized to densify and strengthen a powder compact driven by surface energy reduction. It can be primarily classified into three types: solid-state sintering of crystalline materials, solid-state sintering of amorphous materials or viscous sintering, and liquid phase sintering of crystalline materials. The three types of sintering techniques distinguish themselves by different densification mechanisms.^{1,2} Densification in viscous sintering is achieved by the viscous flow of materials without forming any boundaries or interfaces between the particles. The thermodynamic driving force for the process is the reduction in the total surface energy of a powder aggregate. Sintering through viscous flow has broad

applications in engineering such as densification of low-temperature-co-fired ceramics³ and selective laser sintering of polymer powder bed.⁴

For viscous sintering, most of the existing works have primarily been focused on the neck growth and shrinkage of two glass spheres as a benchmark example. Frenkel was the first to propose an analytical model for the shape evolution of two spherical particles during coalescence.⁵ The proposed model is based on a mechanical energy balance by equating the work of surface tension and the work of dissipation of mechanical energy due to viscous flow and is limited to the early stage of viscous sintering. Eshelby modified Frenkel's model by assuming biaxial extensional flow.⁶ Pokluda et al⁷ further improved the model by approximating the neck growth in all stages of sintering.

Hopper⁸ derived an analytical solution for the coalescence of two equally sized cylinders using a complex variable theory for biharmonic functions. Olevsky et al⁹ have obtained expressions for bulk modulus, sintering stress and densification kinetics as functions of porosity and strain rate sensitivity for nonlinear viscous materials. By employing a simple first-order iterative procedure, the derived formula can be a valuable extension of the continuum theory of sintering. Wakai et al^{10,11} have analyzed the sintering force of two sphere particles by employing the incompressible Stokes equation. They found that the sintering force can be evaluated from the neck growth rate. They also derived sintering mechanics for coupled grain boundary and surface diffusion.¹²

Computationally, various numerical approaches have been employed for modeling viscous sintering, including finite element method (FEM),^{13–17} boundary integral method,¹⁸ boundary element method (BEM),^{19–22} fractional volume of fluids,^{23,24} lattice Boltzmann method.^{25,26} Ross et al²⁷ were the first to introduce FEM to study the sintering process of an infinite line of cylinders. Their solution confirmed that Frenkel's model is not suitable for the whole stages of sintering. Kuiken employed the BEM to simulate the moderate curvature-gradient driven coalescence of viscous particles.¹⁹ Van de Vorst²⁰ also used BEM to analyze the shrinkage of two equal or unequal spheres, and the predicted shrinkage rate matched very well with the corresponding two-dimensional analytic solutions. Kirchhof et al²⁴ applied the fractional volume of fluids to investigate the viscous flow sintering of different agglomerate particle morphologies and found that different sintering contacts in agglomerates even during the first stage of sintering are not completely independent of each other. Gross et al²⁵ employed the lattice Boltzmann method to examine the coalescence of two resting liquid droplets in a saturated vapor phase. Their predictions differ from the existing analytical theories. However, a simple scaling argument, similar to Frenkel's analysis, is proposed that describes simulation results well.

The phase-field method (PFM) has been proven to be a powerful tool to simulate microstructure evolution in a wide variety of materials processes, such as solid-state phase transformations,²⁸ grain growth and coarsening,²⁹ dislocation dynamics,³⁰ dendrite formation in Li-ion batteries,³¹ crack propagation³² and microstructure evolution in thin films,³³ just to name a few. In particular, the phase-field method has been applied to simulate microstructure evolutions in solid-state sintering^{34–38} and liquid phase sintering.³⁹ The difference in employing PFM in different sintering processes lies in the corresponding sintering mechanisms. For example, Wang developed a pioneering phase-field model for solid-state sintering to incorporate various diffusion mechanisms and possible rigid-body

translation and rotation of powder particles.³⁴ However, dissolution and precipitation may have to be considered due to the presence of a liquid phase in liquid phase sintering.³⁹ A more detailed discussion on phase-field models for microstructure evolutions can be found in several excellent review papers.^{40–42}

The present work proposes a thermodynamically consistent phase-field model to study the particle coalescence in viscous sintering. The proposed model is based on an energetic variational formulation.^{43,44} As such, the employed governing equations can be derived consistently under the energy law and the principle of least action. To the best of our knowledge, this is the first phase-field model for viscous sintering by employing a variational principle.

The rest of this paper is organized as follows. Section 2 introduces the proposed framework and illustrates its consistency with thermodynamics. Section 3 qualitatively validates the proposed approach by comparing to theoretical analysis. Section 4 presents several numerical examples to demonstrate the capability of the proposed model to capture the effect of particle shape, initial angle between contacting particles and rearrangement on the viscous sintering behavior. Section 5 concludes with closing remarks on the performance of the proposed approach and discussion on future research work.

2 | GOVERNING EQUATIONS

In the phase-field method, the microstructure evolution is captured by means of a set of phase-field variables that are continuous functions of time and spatial coordinates. These phase-field variables change smoothly but rapidly across interface regions and are generally classified into two groups: conserved and nonconserved variables (or order parameters). Conserved order parameters are typically related to local composition and have to satisfy local conservation condition. The evolution of conserved variables is described by the Cahn-Hilliard diffusion equation. Nonconserved variables usually contain information about local material structure and orientation. The evolution of nonconserved order parameters is governed by the Allen-Cahn equation.

For viscous sintering, as schematically shown in Figure 1A, a conserved order parameter C is introduced to differentiate the powder compact (red region) from the surrounding medium (usually vapor phase) (blue area). Physically, C can be thought as a composition that has an equilibrium value of 1 in amorphous particles and of 0 in the surrounding medium. Assuming constant sintering temperature, the total energy Π of the system consists of two components: Helmholtz free energy \mathcal{F} and kinetic energy \mathcal{K} , which can be expressed as follows:

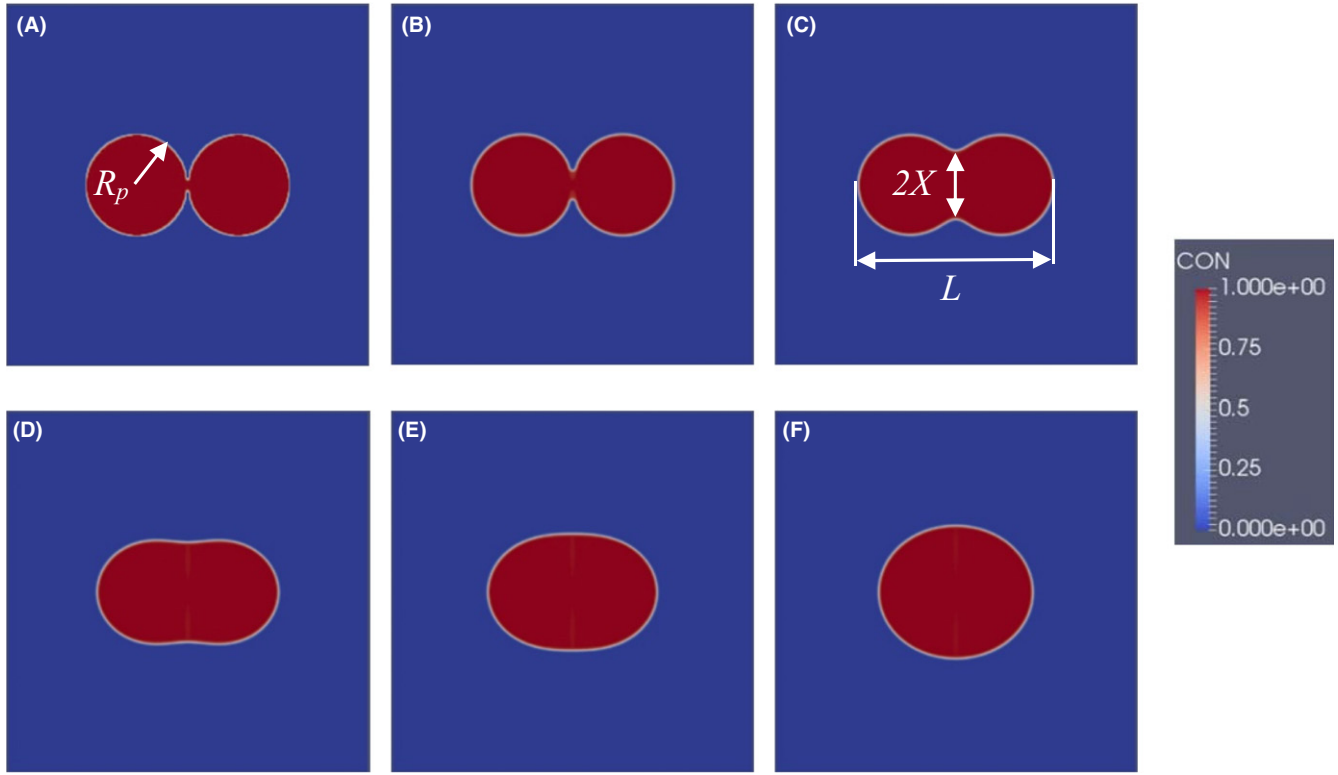


FIGURE 1 Microstructure evolution of two equally sized particles with radius $R_p = R_0$ in 2D at (A) 1000, (B) 10 000, (C) 40 000, (D) 80 000, (E) 120 000, and (F) 200 000 timesteps, respectively. R_p is the initial particle radius, X represents the contact radius and L defines the distance between two particles. Red color denotes the particle compact with the introduced phase-field order parameter C . The “CON” in the color bar represents the order parameter C having a value of 1 within particle compact and of zero within the surrounding medium represented by blue color (See the color bar). This coloring scheme is consistently employed throughout the work if not otherwise mentioned

$$\mathcal{F} = \int_{\Omega} \left[f(C) + \frac{1}{2} k_c \|\nabla C\|^2 \right] d\Omega \quad (1)$$

$$\mathcal{K} = \int_{\Omega} \frac{1}{2} \rho \|\mathbf{v}\|^2 d\Omega \quad (2)$$

$$\Pi = \mathcal{K} + \mathcal{F} = \int_{\Omega} \left[\frac{1}{2} \rho \|\mathbf{v}\|^2 + f(C) + \frac{1}{2} k_c \|\nabla C\|^2 \right] d\Omega \quad (3)$$

In Equation (1), $f(C)$ is a so-called double-well potential as a function of order parameter C . The double-well potential reaches minimum at the corresponding value of C in each phase and is employed as $f(C) = AC^2(1 - C)^2$ in the present work. Let Γ_t represent the total surface area of the evolving powder compact and γ be the constant isotropic-specific surface energy (surface tension). We note that \mathcal{F} is essentially a phase-field approximation of surface energy $\Gamma_t \gamma$ with an accuracy determined by the width ε of the interface between particle aggregates and the surrounding medium. Mathematically, it has been rigorously proven that $\mathcal{F} \rightarrow \Gamma_t \gamma$ as $\varepsilon \rightarrow 0$.^{45,46} Parameters A and k_c can be determined from γ and ε ⁴³ as $A = \frac{3\gamma}{8\sqrt{2}\varepsilon}$ and $K_c = \frac{3\gamma\varepsilon}{2\sqrt{2}}$. $\|\cdot\|$ represents the L^2 norm for a vector object.

In Equation (2), \mathbf{v} is the velocity vector field. Density ρ of the mixed system can be calculated as:

$$\rho = \rho_{\text{vapor}} + (\rho_{\text{particle}} - \rho_{\text{vapor}})N(C), \quad (4)$$

where ρ_{vapor} and ρ_{particle} represent the densities of surrounding medium phase and powder particles, respectively, and $N(C)$ is an interpolation function of phase-field variable C with $N(1) = 1$ in particle compact and $N(0) = 0$ in vapor phase.

The driving force for viscous sintering is to minimize the total energy of particle compact through energy dissipation by viscous flow.² As such, the energy dissipation law for isothermal viscous sintering process can be expressed as:

$$\frac{d\Pi}{dt} = \frac{d(\mathcal{K} + \mathcal{F})}{dt} = - \int_{\Omega} 2\mu(C) \left\| \frac{\nabla \mathbf{v} + (\nabla \mathbf{v})^T}{2} \right\|^2 d\Omega, \quad (5)$$

where $\|\cdot\|$ denotes the Hilbert-Schmidt or the Frobenius norm for a tensor object, and μ is the viscosity of the mixed system and can be expressed as:

$$\mu = \mu_{\text{vapor}} + (\mu_{\text{particle}} - \mu_{\text{vapor}})N(C), \quad (6)$$

where μ_{vapor} and μ_{particle} are viscosities of the respective surrounding vapor phase and viscous particles.

Under the energy dissipation law defined in Equation (5) and assuming the system is incompressible, governing equations for viscous sintering can be derived following the energetic variational approach⁴³:

$$\frac{\partial C}{\partial t} = \nabla \cdot \left[M \nabla \left(\frac{\delta \Pi}{\delta C} \right) \right] - \nabla \cdot (\mathbf{v}C) \quad (7)$$

$$\rho \left[\frac{\partial \mathbf{v}}{\partial t} + (\mathbf{v} \cdot \nabla) \mathbf{v} \right] = -\nabla p + \nabla \cdot [\mu(C)(\nabla \mathbf{v} + (\nabla \mathbf{v})^T)] - \nabla \cdot \left(\frac{\partial \Pi}{\partial \nabla C} \otimes \nabla C \right) \quad (8)$$

$$\nabla \cdot \mathbf{v} = \mathbf{0} \quad (9)$$

Equation (7) is essentially a modified Cahn-Hilliard equation by incorporating convection flux and M is a small relaxation parameter. We note that energy dissipation through the relaxation term in Equation (7) is not included in the energy law defined in Equation (5). The reason is that energy dissipation through viscous flow dominates. A more comprehensive energy law considering energy dissipation through relaxation can be found in⁴³ and Equation (7) can be derived under such a comprehensive law. Equation (8) is the Navier-Stokes equation that physically describes the balance of linear momentum. The Lagrange multiplier p accounting for incompressibility adds the pressure term $-\nabla p$ to the force balance. Variation of energy dissipation with respect to the velocity field produces $\nabla \cdot [\mu(C)(\nabla \mathbf{v} + (\nabla \mathbf{v})^T)]$ as the dissipative force. The term $-\nabla \cdot \left(\frac{\partial \Pi}{\partial \nabla C} \otimes \nabla C \right)$ in Equation (8) physically represents the surface tension contribution to the balance of linear momentum in the proposed phase-field or diffuse interface model and can be mathematically derived by taking the variation of the Helmholtz free energy (or surface energy) defined in Equation (1) with respect to spatial positions of particles. The detailed derivation of the surface tension contribution can be found in.⁴³ Equation (9) represents a mathematical description of incompressibility, and conservation of mass is satisfied under this condition with the assumption that mass density is uniform initially within the particle compact. As such, the proposed phase-field model is thermodynamically consistent in the sense that conservation of mass is satisfied, and that balance of linear momentum is derived under the energy dissipation law defined in Equation (5).

3 | VALIDATION

To qualitatively validate the proposed phase-field model in Section 2, the classical benchmark problem of viscous sintering of two equally sized circular particles in

two-dimension (2D) is employed. The simulation domain Ω is set to be $\Omega = (0, 2\pi)^2$ and periodic boundary conditions are applied in all directions. In the simulation, the inertia term in Equation (8) is negligible since small particles with relatively high viscosity are considered, as employed in the theoretical analysis¹¹ and computer simulation.¹³ In addition, the viscosity for the system is assumed to be uniform and an arithmetically averaged viscosity between particle and surrounding medium is employed. Material properties of polyamide 12 (PA12)¹³ such as surface tension γ and viscosity μ at temperature $T = 175^\circ\text{C}$ are employed as $\gamma = 0.03\text{N/m}$ and $\mu = 400$ Pa.s. The normalized time t^* is defined as $t^* = \frac{\gamma t}{R_p \mu}$ where t represents the real time and R_p the initial particle radius, as employed in.^{11,13} Equations (7-9) are spatially discretized by a 256×256 uniform grid. The spectral method using second-order semi-implicit discretization in time⁴⁷ is employed with a normalized timestep $\Delta t^* = 1.25e-5t^*$. The relaxation parameter M in Equation (7) is chosen to be $M = 1e-6$ and the interfacial thickness ε is chosen to be

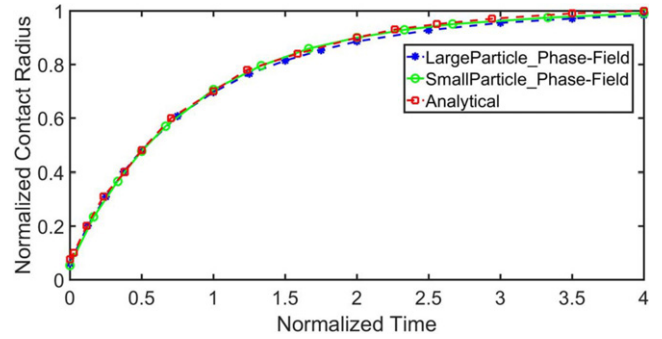


FIGURE 2 Normalized contact radius as a function of normalized time for viscous sintering of the respective theoretical analysis (red), two equally sized particles with relatively large (blue) and small (green) radius in 2D

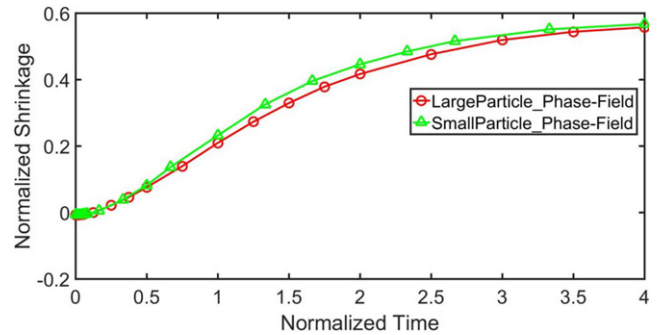


FIGURE 3 Normalized shrinkage as a function of the normalized time for viscous sintering of the respective particle sizes

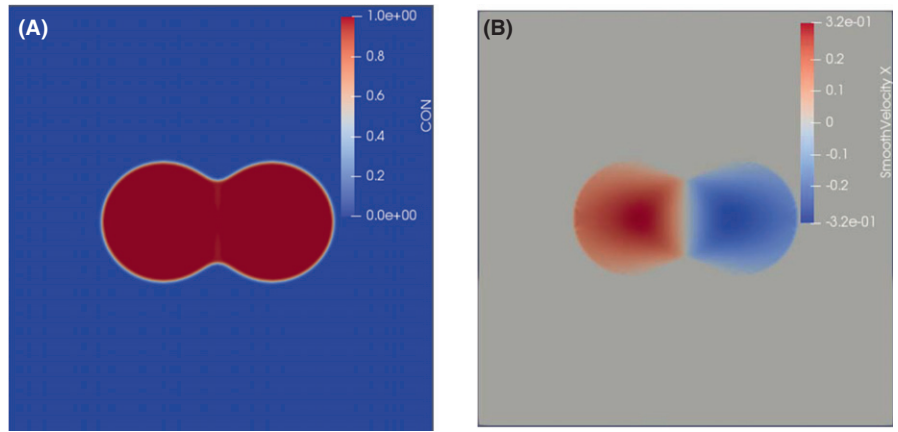


FIGURE 4 A, The shape of the particle compact and (B) the distribution of the axial velocity field inside the particle compact along x (horizontal) direction at $t^* = 0.5$

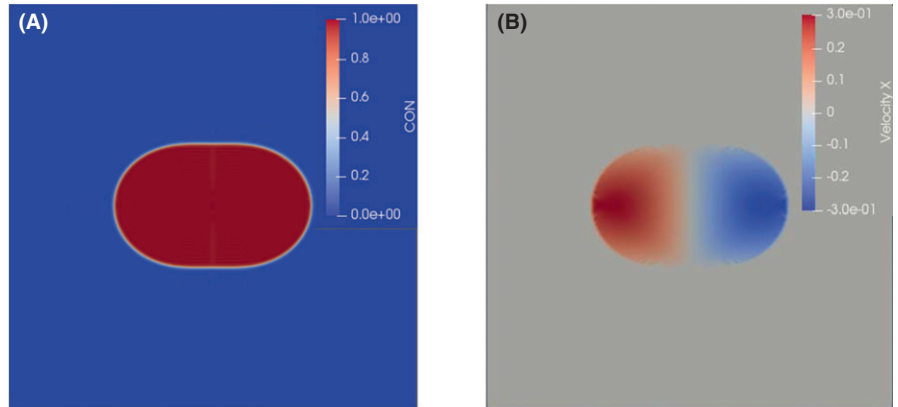


FIGURE 5 A, The shape of the particle compact and (B) the distribution of velocity field inside the particle compact along x (horizontal) direction at $t^* = 1.25$

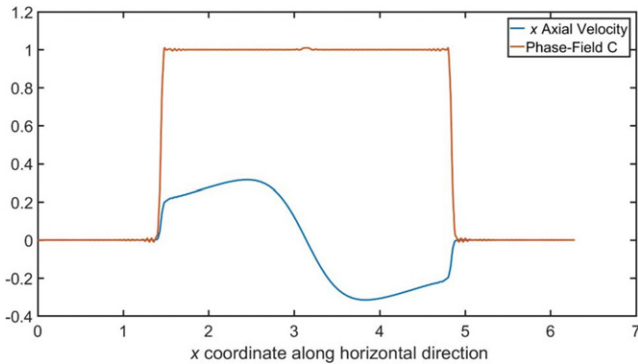


FIGURE 6 The distributions of the introduced phase-field C and the velocity field within the particle compact in x (horizontal) direction along the axis connecting the centers of the two particles at $t^* = 0.5$. The phase-field C is unitless and the velocity has a unit of $\frac{\gamma}{\mu}$, where γ is the employed surface tension and μ the viscosity

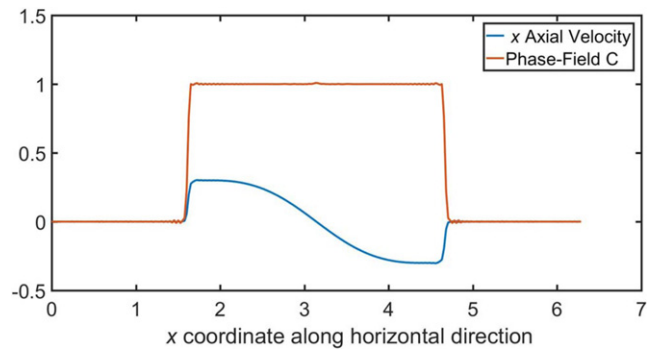


FIGURE 7 The distributions of the introduced phase-field C and the velocity field within the particle compact in x (horizontal) direction along the axis connecting the centers of the two particles $t^* = 1.25$. The phase-field C is unitless and the velocity has a unit of $\frac{\gamma}{\mu}$, where γ is the employed surface tension and μ the viscosity

$3h$ where h represents the spacing between two spatial grid points.

As denoted in Figure 1, let X represent the contact radius and R_p be the initial particle radius. The normalized contact radius $\frac{X}{R_p}$ is plotted as a function of the normalized time t^* and is compared to the Hopper's analytical solution^{8,13} in Figure 2. The definition of the normalized time t^* represents the scaling law in terms of surface tension,

viscosity and particle size. As such, the neck growth curve with respect to different particle sizes can be obtained for given surface tension and viscosity. In this section, two equally sized particles with initial particle radius $R_p = R_0$ and $R_p = 0.75R_0$ are employed, respectively. It can be observed from Figure 2 that for both particle sizes, the contact radius growth behavior captured by the proposed phase-field model matches very well with that from the

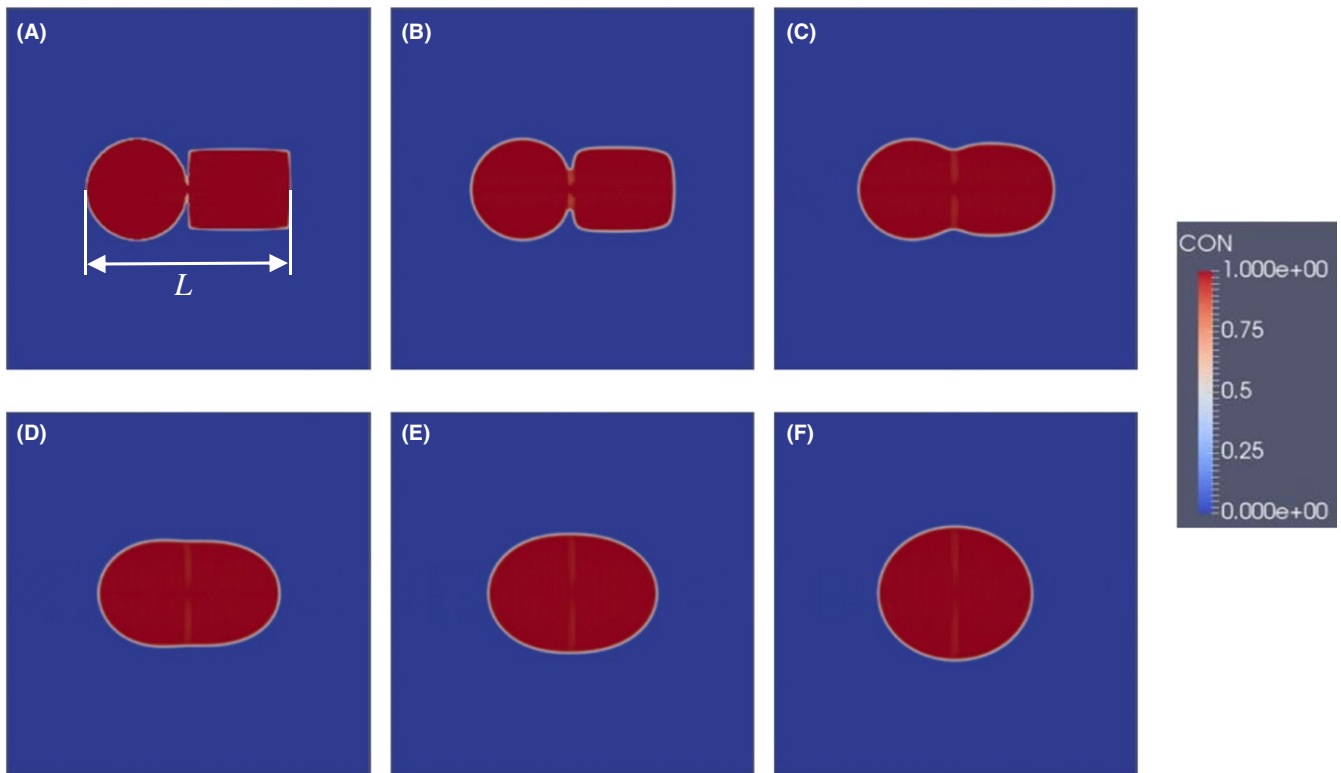


FIGURE 8 Microstructure morphology of the employed circle-rectangle particle compact in 2D at (A) 1000, (B) 10 000, (C) 40 000, (D) 80 000, (E) 120 000, and (F) 200 000 timesteps, respectively

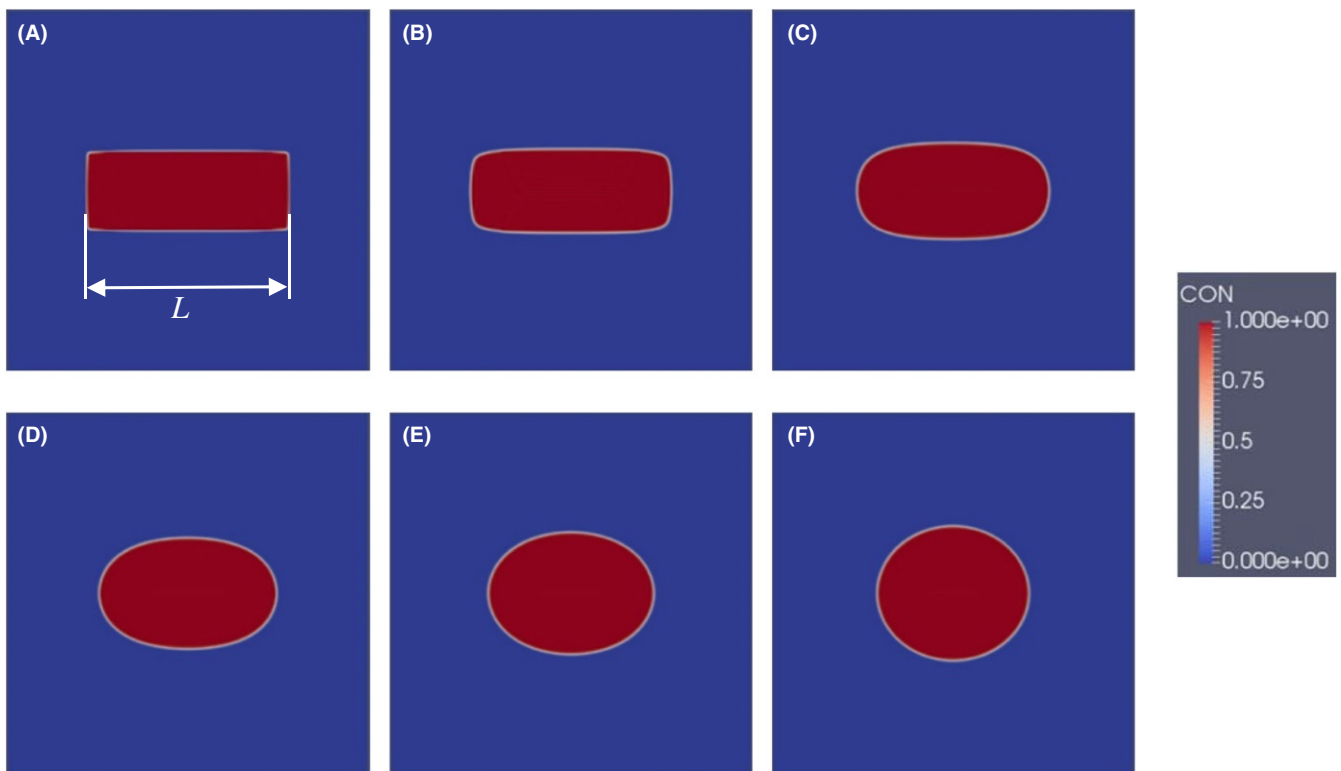


FIGURE 9 Microstructure evolution of the employed rectangle-rectangle particle compact in 2D at (A) 1000, (B) 10 000, (C) 40 000, (D) 80 000, (E) 120 000, and (F) 200 000 timesteps, respectively

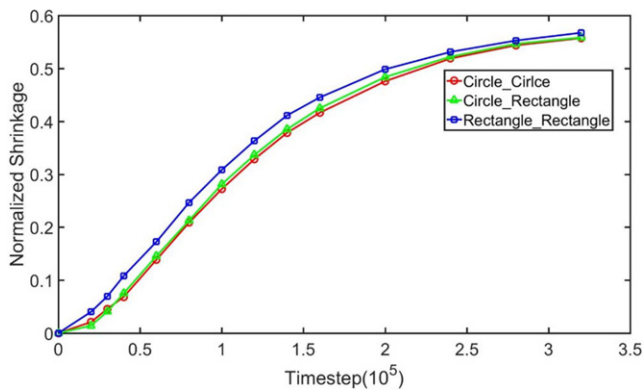


FIGURE 10 Normalized shrinkages at different timesteps for viscous sintering of the respective circle-circle (red), circle-rectangle (green), and rectangle-rectangle (blue) compacts

theoretical analysis. The contact radius increases as time proceeds, with a decreasing growth rate due to the reduction of driving force. The predicted normalized contact radius $\frac{x}{R_p}$ is 1.412 at equilibrium. It matches very well with the theoretical value $\sqrt{2}$, which can be derived from the conservation of area in 2D. Figure 1 shows snapshots from the phase-field simulation at different timesteps for the employed two equally sized particles with a larger radius. The “CON” in the color bar represents the introduced conserved phase-field variable C ranging from 0 to 1.

The normalized shrinkages as a function of normalized time for $R_p = R_0$ and $R_p = 0.75R_0$ are shown in Figure 3.

Let L be the distance between two particles, as defined in Figure 1. Then the normalized shrinkage can be defined as: $\frac{\Delta L}{2R_p} = \frac{4R_p - L}{2R_p}$ with ΔL being the distance change. The unity of the two shrinkage curves with respect to the corresponding particles sizes is reproduced qualitatively with a slight difference between them. The difference may be introduced due to the diffuse-interface (phase-field) approximation. For example, the same interfacial thickness and discretization grid are employed for both particle sizes. The shrinkage increases as time proceeds, with an overall decreasing rate. Similar to contact radius growth, the decrease in driving force with time may account for the decreasing shrinkage rate. We note that the predicted normalized shrinkage at equilibrium is 0.582 for both particle sizes, which is in good agreement with the theoretical value $2 - \sqrt{2} \cong 0.583$.

The velocity profile v_x inside the particle compact along the x (horizontal) direction and the corresponding shape of the particle compact at $t^* = 0.5$ and $t^* = 1.25$ are shown in Figures 4 and 5, respectively. In Figures 4B and 5B, since the velocity distribution within the particle compact is of interest, the velocity profile is achieved by calculating the product Cv_x , where C is the introduced order parameter, to smear out the velocity in the surrounding vapor phase and to better visualize v_x inside the particle compact. Figures 6 and 7 plot the distribution of Cv_x and the profile of the phase-field C along the axis connecting the centers of the two particles at $t^* = 0.5$ and $t^* = 1.25$, respectively. From the symmetry, the point at $x = \pi$ where the contact plane is

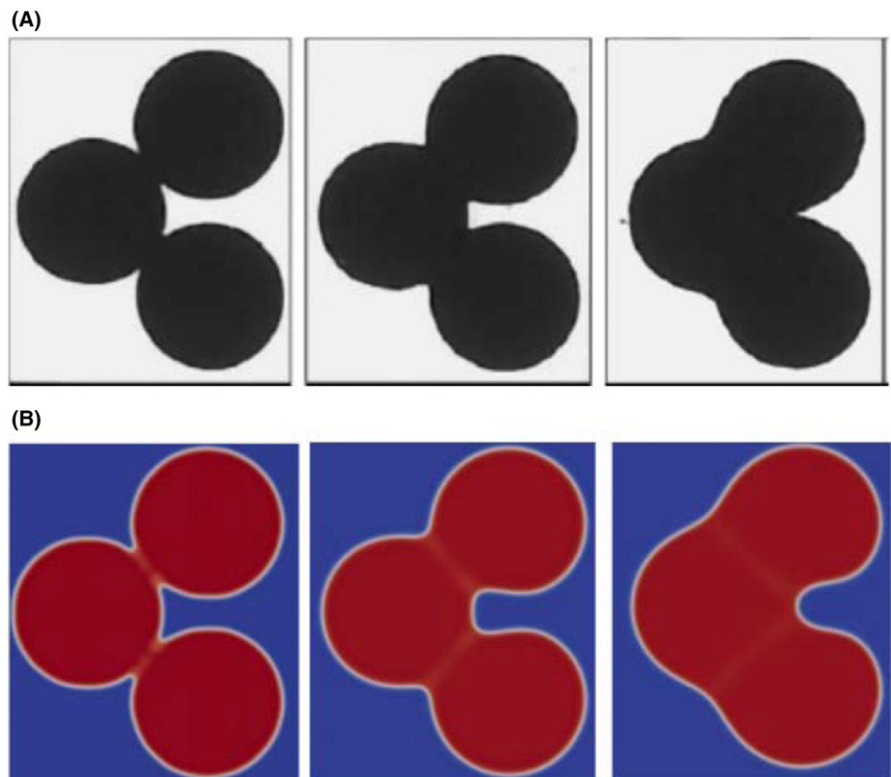


FIGURE 11 Microstructure morphologies of a three-particle compact from experimental observations (A) (reproduced with permission from John Wiley and Sons) and phase-field predictions (B)

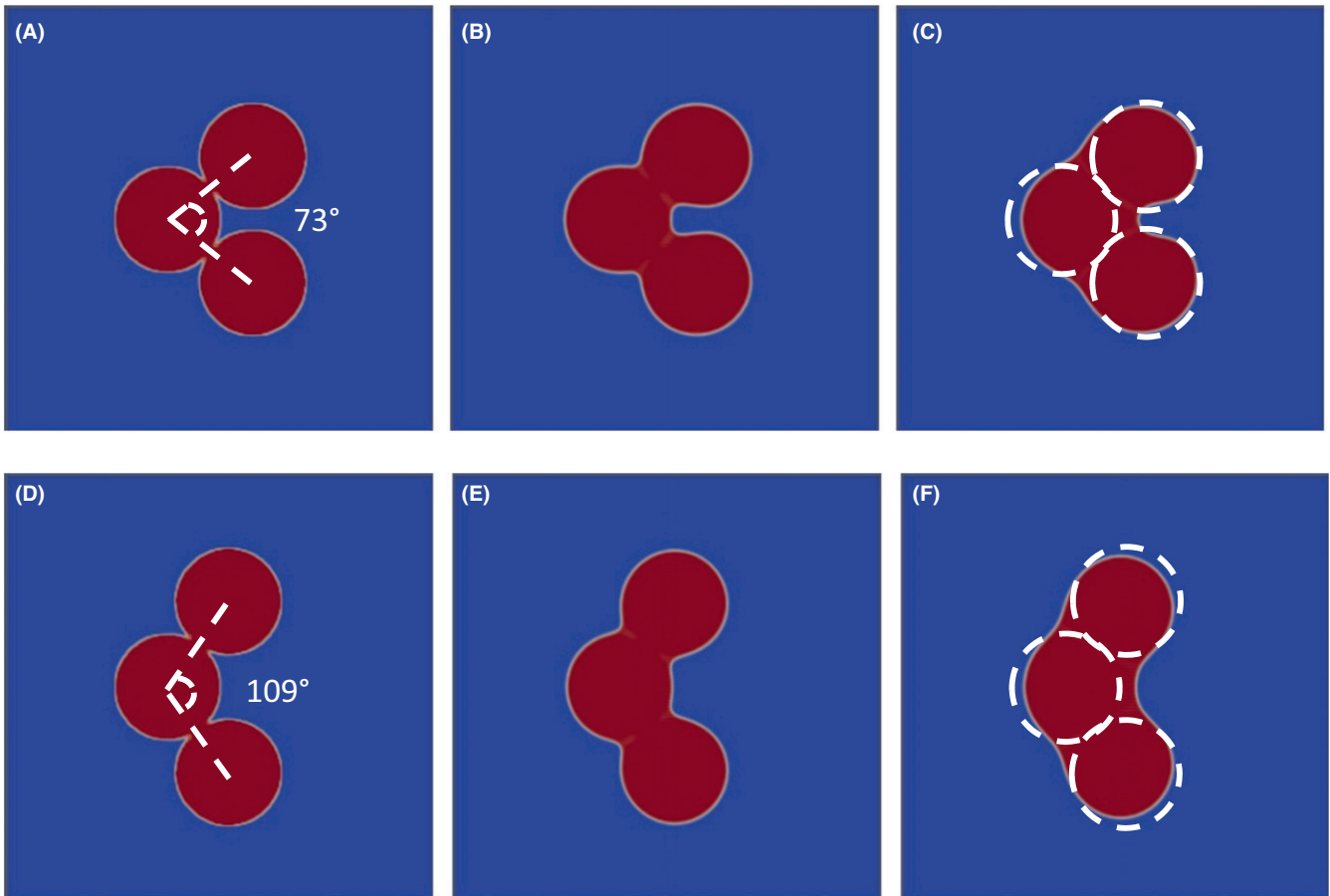


FIGURE 12 Microstructure evolution and the corresponding angle change for the employed three-particle compacts with initial contact angles 73° (A-C) and 109° (D-F) at the same timesteps. The dashed outlines in (C) and (F) represent the initial configurations of the respective particle compacts

located is a stagnation point. At the later stage of viscous sintering, the axial velocity field is approximately divided into two regions: the straining region close to the stagnation point where the axial velocity is linearly proportional to the distance from the stagnation point with a slope equal to the axial strain rate and the so-called rigid body motion region where the axial velocity is close to constant. The axial velocity distribution pattern inside the particle compact matches very well with that in the theoretical analysis,¹¹ which qualitatively validates the proposed phase-field model.

4 | NUMERICAL EXAMPLES

In this section, the proposed phase-field model is employed to investigate the effects of particle shape and initial contact angle on viscous sintering of glass particles. To demonstrate the effectiveness of the phase-field approach to capture the morphology of complex microstructures, a many-particle system with irregular green structure is employed. The simulation results are compared with experimental observations qualitatively.

4.1 | Particle shape effect

In order to investigate particle shape effect on viscous sintering, two-particle models with the respective circle-circle contact (Figure 1), circle-rectangle contact (Figure 8), and rectangle-rectangle contact (Figure 9) are employed and compared with each other. The aforementioned three models are designed such that the rectangle particle has the same area as the employed circle and that each model has the same initial length L_0 . The normalized shrinkage for each model is plotted in Figure 10. It is demonstrated that the rectangle-rectangle compact has the fastest shrinkage rate with the circle-rectangle aggregates having the moderate and the circle-circle model having the slowest, though the difference between the last two models is small. The predicted particle shape effect also matches well with the experimental observation.⁴⁸ Since the employed rectangle and circle particles have the same area, the nonequilibrium particle shape (rectangle) has more driving force (more perimeter in 2D) than the equilibrium shape (circle in 2D). As such, particles with nonequilibrium shapes sinter faster than equilibrium particle shapes. We note that particle shape effect may be more

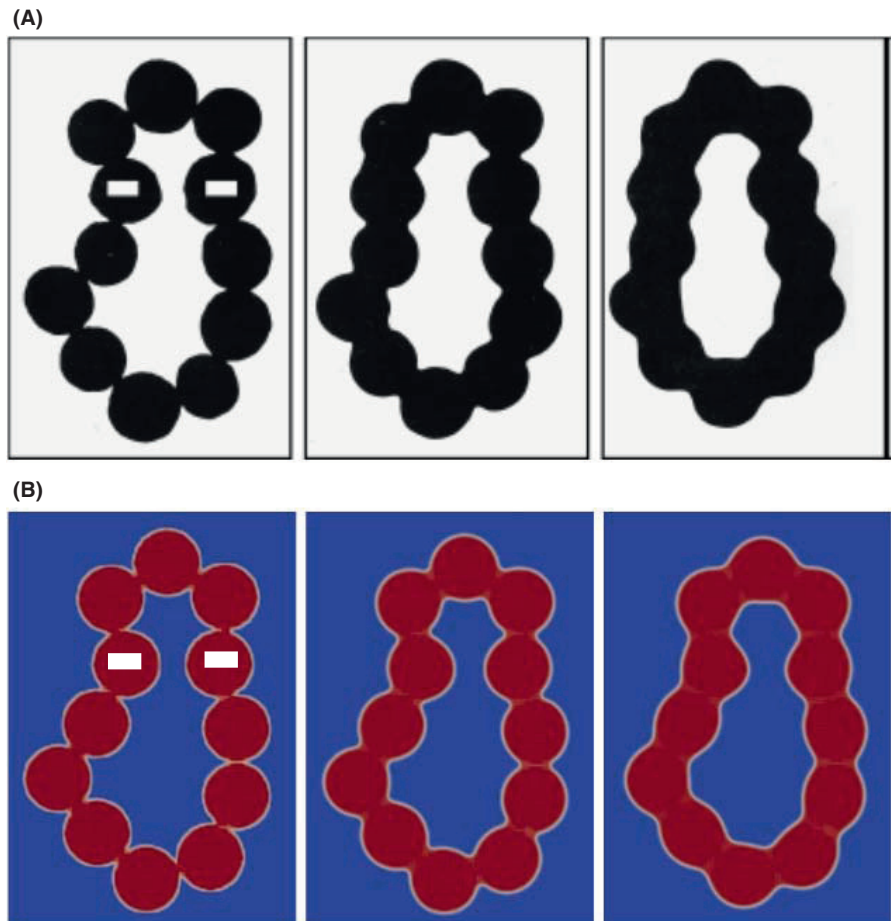


FIGURE 13 Particle rearrangement of the employed many-particle chain from experimental observations (A) (reproduced with permission from John Wiley and Sons) and phase-field simulations (B)

significant for many-particle models having complex green structures and will be left for future study.

Microstructure evolutions for the employed circle-rectangle and rectangle-rectangle models are shown in Figures 8 and 9, respectively. Both models will reach the same equilibrium state to form a larger circle with different sintering rates.

4.2 | Initial contact angle effect

The three-particle models with different initial contact angles in the experimental study⁴⁹ have been employed for the phase-field simulation. The three-particle compact with an initial angle of 73° is firstly used to compare with the experimental observations.⁴⁹ Due to the lack of information on material properties for glass particles employed in the experiment, a qualitative comparison is performed. As shown in Figure 11, PFM has the capability to qualitatively reproduce the morphologies of the three-particle model observed in the experiment.

Microstructure evolutions of three-particle compacts with two different initial contact angles are compared with each other in Figure 12. The dashed lines represent the initial configurations of the respective particle models. It is observed that with a relatively smaller initial angle, the

particle in the middle moves more toward the right, which has a tendency to open up the particle compact and that with a relatively larger initial angle, the particle on the top flows more downwards and the bottom particle proceeds more upwards, which tends to close up the model. This is due to the fact that the sintering force between particles along the axis connecting particle centers has a larger projection along horizontal direction with the relatively smaller initial angle and has a larger component in the vertical direction with a relatively larger initial angle. As such, the three-particle compact with a small initial contact angle opens up more and has a larger angle change, which matches the experimental observations.⁴⁹

4.3 | Many particles simulation

A many-particle compact with the irregular arrangement, as shown in Figure 13, is employed to demonstrate the capability of PFM to model systems with a complex green structure. The particle chain is designed such that it has a similar initial structure as the one used in an experimental study.⁴⁹ As shown in Figure 13, the stretching of the particle compact leads to an increasing distance between the two marked particles (with rectangle boxes) in the top part of the chain and a decrease in the maximum dimension of

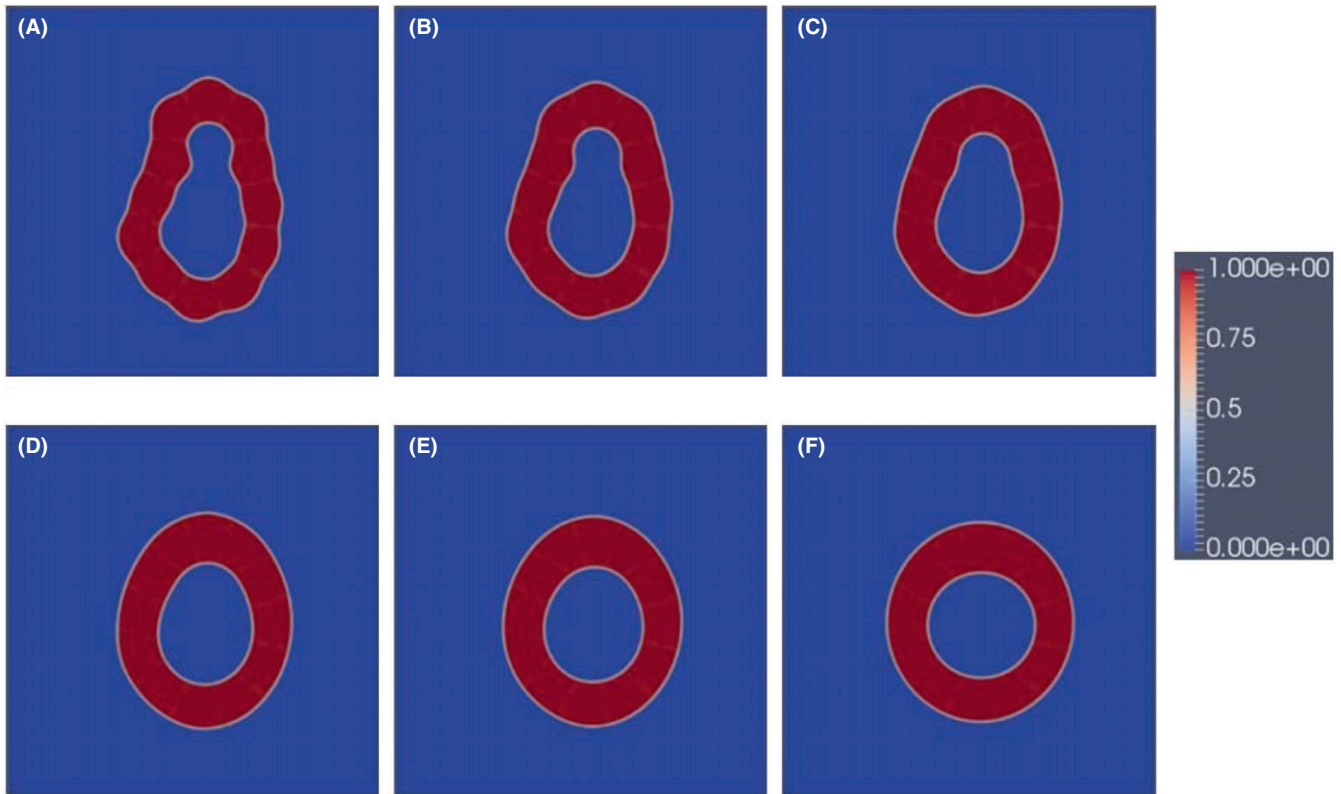


FIGURE 14 Microstructure morphologies of the employed many-particle chain at (A) 30 000, (B) 40 000, (C) 50 000, (D) 80 000, (E) 100 000, and (F) 200 000 timesteps, respectively

the pore area included by the particle compact, which qualitatively reproduces what is observed in the experiment. As analyzed in Figure 12, the marked particle on the left-hand side has a sintering force projection along the negative horizontal direction and the marked particle on the right-hand side has a sintering force component along the positive horizontal direction due to the corresponding particle arrangement nearby or different initial contact angles. The discrepancy may be induced by the difference in green structures employed in PFM and experiment (for instance, initial angles between connecting particles and particle shapes).

Figure 14 shows some further snapshots of microstructure morphology from PFM simulation. It is demonstrated that the elongated pore tends to change shapes to rounded one by changing the angles between contacting particles and that the maximum dimension of the pore area is decreasing until the particle chain reaches a donut-like equilibrium shape such that the total surface area is minimized. We note that the closed pore will not disappear due to the fact that the vapor pressure in the pore can just balance out the surface tension, as mentioned in the theoretical analysis in.⁵⁰

We note that the computational cost involved in modeling the many-particle system is identical to that required in a single particle simulation, as long as the domain sizes of

different systems are the same in PFM. The morphology of arbitrary green structures can be captured using the PFM without explicitly tracking positions of moving interfaces, as in modeling particle systems with simplified geometries. In addition, the proposed PFM has a dimensional generality since the employed governing equations are not aware of dimensionality. As such, it can be organically extended to three-dimension (3D).

5 | CONCLUSION

In this work, we have proposed a phase-field model for viscous sintering. Microstructure evolution of glass particle compact is implicitly captured by the evolution of a conserved order parameter to differentiate particles from surrounding medium. The viscous flow is governed by the Stokes equation coupled with surface tension effect. Governing equations in the model can be analytically derived under the energy law employing the energetic variational approach, which makes the proposed model thermodynamically consistent.

To qualitatively validate the proposed PFM, the normalized contact radius growth as a function of normalized time from PFM is compared with that from theoretical analysis, employing a two- equally sized circular particle model with

different radius in 2D. The predicted normalized contact radius matches well with their theoretical counterparts. Then the proposed PFM was applied to study the effect of particle shape and initial contact angle on sintering of glass particles. A many-particle model with irregular arrangement has also been employed to demonstrate the capability of PFM to simulate microstructure evolution with a complex green structure. The morphologies of different particle compacts from PFM simulations have good agreement with experimental observations qualitatively. We note that the proposed approach can be readily and consistently generalized to three-dimension.

In the future, several research directions will be pursued. First, glass particles with viscoelastic behavior will be considered to study the effect of viscoelasticity on the microstructure evolution in viscous sintering. Depending on the employed constitutive model, elastic energy will be considered in the total free energy. Second, particles with varying material properties such as viscosity will be examined. Finally, the proposed phase-field approach can be extended to model solid-state sintering by adding grain boundary energy contribution to the total energy and to simulate liquid phase sintering and the novel cold sintering technique⁵¹ by considering the dissolution-precipitation process, with the ultimate goal to establish a robust and unified phase-field model for different sintering techniques.

ACKNOWLEDGMENTS

This work is supported by the Department of Energy through ARPA-E grant DE-AR0000766 (Q. Yang and L. Chen) and by the Hamer Foundation for the Hamer Professorship (L. Chen) and by the National Science Foundation through grant DMS-1720442 (J. Shen) and DMS-1759536 (A. Kirshtein and C. Liu) and by the Air Force Office of Scientific Research through FA9550-16-1-0102 (J. Shen).

ORCID

Qingcheng Yang  <http://orcid.org/0000-0001-5321-801X>

REFERENCES

- Bordia RK, Kang SJL, Olevsky EA. Current understanding and future research directions at the onset of the next century of sintering science and technology. *J Am Ceram Soc.* 2017;100(6):2314–52.
- German R. *Sintering: from empirical observations to scientific principles.* Oxford: Butterworth-Heinemann; 2014.
- Kemethmüller S, Hagymasi M, Stiegelschmitt A, Roosen A. Viscous flow as the driving force for the densification of low-temperature co-fired ceramics. *J Am Ceram Soc.* 2007;90(1):64–70.
- Schmid M, Amado A, Wegener K, editors. *Polymer powders for selective laser sintering (SLS).* AIP Conference Proceedings; 2015: AIP Publishing.
- Frenkel J. Viscous flow of crystalline bodies under the action of surface tension. *J Phys(USS R).* 1945;9(5):385.
- Eshelby JD. Discussion of “Seminar on the kinetics of sintering”. *Trans Am Inst Met Engrs.* 1949;185(11):796–813.
- Pokluda O, Bellehumeur CT, Vlachopoulos J. Modification of Frenkel's model for sintering. *AIChE J.* 1997;43(12):3253–6.
- Hopper RW. Plane Stokes flow driven by capillarity on a free surface. *J Fluid Mech.* 1990;213:349–75.
- Giuntini D, Olevsky EA. Sintering stress of nonlinear viscous materials. *J Am Ceram Soc.* 2016;99(11):3520–4.
- Okuma G, Kadowaki D, Hondo T, Sato A, Tanaka S, Wakai F. Computation of sintering stress and bulk viscosity from microtomographic images in viscous sintering of glass particles. *J Am Ceram Soc.* 2017;100(3):867–75.
- Wakai F, Katsura K, Kanchika S, Shinoda Y, Akatsu T, Shinagawa K. Sintering force behind the viscous sintering of two particles. *Acta Mater.* 2016;109:292–9.
- Wakai F, Brakke K. Mechanics of sintering for coupled grain boundary and surface diffusion. *Acta Mater.* 2011;59(14):5379–87.
- Balemans C, Hulsen MA, Anderson PD. Sintering of two viscoelastic particles: a computational approach. *Appl Sci.* 2017;7(5):516.
- Martínez-Herrera JI, Derby JJ. Analysis of capillary-driven viscous flows during the sintering of ceramic powders. *AIChE J.* 1994;40(11):1794–803.
- Martínez-Herrera JI, Derby JJ. Viscous sintering of spherical particles via finite element analysis. *J Am Ceram Soc.* 1995;78(3):645–9.
- Djohari H, Martínez-Herrera JI, Derby JJ. Transport mechanisms and densification during sintering: I. Viscous flow versus vacancy diffusion. *Chem Eng Sci.* 2009;64(17):3799–809.
- Katsura K, Shinoda Y, Akatsu T, Wakai F. Sintering force behind shape evolution by viscous flow. *J Eur Ceram Soc.* 2015;35(3):1119–22.
- Hiram Y, Nir A. A simulation of surface tension driven coalescence. *J Colloid Interface Sci.* 1983;95(2):462–70.
- Kuiken H. Viscous sintering: the surface-tension-driven flow of a liquid form under the influence of curvature gradients at its surface. *J Fluid Mech.* 1990;214:503–15.
- Van de Vorst G. Numerical simulation of axisymmetric viscous sintering. *Eng Anal Boundary Elem.* 1994;14(2):193–207.
- Van de Vorst G, Mattheij RM, Kuiken HK. A boundary element solution for two-dimensional viscous sintering. *J Comput Phys.* 1992;100(1):50–63.
- Van de Vorst G, Mattheij RMM. Numerical analysis of a 2-D viscous sintering problem with non-smooth boundaries. *Computing.* 1992;49(3):239–63.
- Kirchhof M, Förster H, Schmid H-J, Peukert W. Sintering kinetics and mechanism of vitreous nanoparticles. *J Aerosol Sci.* 2012;45:26–39.
- Kirchhof M, Schmid H-J, Peukert W. Three-dimensional simulation of viscous-flow agglomerate sintering. *Phys Rev E.* 2009;80(2):026319.
- Gross M, Steinbach I, Raabe D, Varnik F. Viscous coalescence of droplets: a lattice Boltzmann study. *Phys Fluids.* 2013;25(5):052101.

26. Varnik F, Rios A, Gross M, Steinbach I. Simulation of viscous sintering using the lattice Boltzmann method. *Modell Simul Mater Sci Eng*. 2013;21(2):025003.
27. Ross J, Miller W, Weatherly G. Dynamic computer simulation of viscous flow sintering kinetics. *J Appl Phys*. 1981;52(6):3884–8.
28. Chen L, Wolverson C, Vaithyanathan V, Liu Z. Modeling solid-state phase transformations and microstructure evolution. *MRS Bull*. 2001;26(3):197–202.
29. Chen L-Q, Yang W. Computer simulation of the domain dynamics of a quenched system with a large number of nonconserved order parameters: the grain-growth kinetics. *Phys Rev B*. 1994;50(21):15752.
30. Wang Y, Jin Y, Cuitino A, Khachaturyan A. Phase field microelasticity theory and modeling of multiple dislocation dynamics. *Appl Phys Lett*. 2001;78(16):2324–6.
31. Chen L, Zhang HW, Liang LY, Liu Z, Qi Y, Lu P, et al. Modulation of dendritic patterns during electrodeposition: a nonlinear phase-field model. *J Power Sources*. 2015;300:376–85.
32. Borden MJ, Verhoosel CV, Scott MA, Hughes TJ, Landis CM. A phase-field description of dynamic brittle fracture. *Comput Methods Appl Mech Eng*. 2012;217:77–95.
33. Li Y, Hu S, Liu Z, Chen L. Phase-field model of domain structures in ferroelectric thin films. *Appl Phys Lett*. 2001;78(24):3878–80.
34. Wang YU. Computer modeling and simulation of solid-state sintering: a phase field approach. *Acta Mater*. 2006;54(4):953–61.
35. Ahmed K, Yablinsky C, Schulte A, Allen T, El-Azab A. Phase field modeling of the effect of porosity on grain growth kinetics in polycrystalline ceramics. *Modell Simul Mater Sci Eng*. 2013;21(6):065005.
36. Chockalingam K, Kouznetsova V, van der Sluis O, Geers M. 2D Phase field modeling of sintering of silver nanoparticles. *Comput Methods Appl Mech Eng*. 2016;312:492–508.
37. Biswas S, Schwen D, Singh J, Tomar V. A study of the evolution of microstructure and consolidation kinetics during sintering using a phase field modeling based approach. *Extreme Mech Lett*. 2016;7:78–89.
38. Kazaryan A, Wang Y, Patton BR. Generalized phase field approach for computer simulation of sintering: incorporation of rigid-body motion. *Scripta Mater*. 1999;5(41):487–92.
39. Villanueva W, Grönhagen K, Amberg G, Ågren J. Multicomponent and multiphase simulation of liquid-phase sintering. *Comput Mater Sci*. 2009;47(2):512–20.
40. Chen L-Q. Phase-field models for microstructure evolution. *Annu Rev Mater Res*. 2002;32(1):113–40.
41. Chen LQ. Phase-field method of phase transitions/domain structures in ferroelectric thin films: a review. *J Am Ceram Soc*. 2008;91(6):1835–44.
42. Moelans N, Blanpain B, Wollants P. An introduction to phase-field modeling of microstructure evolution. *Calphad*. 2008;32(2):268–94.
43. Giga M-H, Kirshtein A, Liu C. Variational Modeling and Complex Fluids. In: Giga Y, Novotny A, editors. *Handbook of mathematical analysis in mechanics of viscous fluids*. Cham: Springer International Publishing, 2017; pp. 1–41.
44. Kwak DY, Hyon Y, Liu C. Energetic variational approach in complex fluids: maximum dissipation principle. *Discrete Continuous Dyn Syst*. 2010;26(4):1291–304.
45. Yue P, Zhou C, Feng JJ. Sharp-interface limit of the Cahn–Hilliard model for moving contact lines. *J Fluid Mech*. 2010;645:279–94.
46. Magaletti F, Picano F, Chinappi M, Marino L, Casciola CM. The sharp-interface limit of the Cahn–Hilliard/Navier–Stokes model for binary fluids. *J Fluid Mech*. 2013;714:95–126.
47. Chen LQ, Shen J. Applications of semi-implicit Fourier-spectral method to phase field equations. *Comput Phys Commun*. 1998;108(2–3):147–58.
48. Cutler IB, Henrichsen RE. Effect of particle shape on the kinetics of sintering of glass. *J Am Ceramic Soc*. 1968;51(10):604.
49. Exner HE, Mueller C. Particle rearrangement and pore space coarsening during solid-state sintering. *J Am Ceram Soc*. 2009;92(7):1384–90.
50. Mackenzie J, Shuttleworth R. A phenomenological theory of sintering. *Proc Phys Soc London, Sect B*. 1949;62(12):833.
51. Guo J, Guo H, Baker AL, Lanagan MT, Kupp ER, Messing GL, et al. Cold sintering: a paradigm shift for processing and integration of ceramics. *Angew Chem Int Ed*. 2016;55(38):11457–61.

How to cite this article: Yang Q, Kirshtein A, Ji Y, Liu C, Shen J, Chen L-Q. A thermodynamically consistent phase-field model for viscous sintering. *J Am Ceram Soc*. 2018;00:1–12. <https://doi.org/10.1111/jace.16021>